Low-Frequency Variability in a Turbulent Baroclinic Jet: Eddy–Mean Flow Interactions in a Two-Level Model

JOSEPH BERNSTEIN AND BRIAN FARRELL

Harvard University, Cambridge, Massachusetts

(Manuscript received 6 April 2009, in final form 12 June 2009)

ABSTRACT

The origin of low-frequency variability in the midlatitude jet is investigated using a two-level baroclinic channel model. The model state fields are separated into slow and fast components using intermediate time-scale averaging. In the equation for the fast variables the nonlinear wave–wave interactions are parameterized as a stochastic excitation. The slowly varying ensemble mean eddy fluxes obtained from the resulting stochastic turbulence model are coupled with the slowly varying mean flow dynamics. This forms a coupled set of deterministic equations on the slow time scale that governs the dynamics of the eddy–mean flow interaction. The equilibria of this coupled system are found as a function of the excitation strength, which controls the level of turbulence. At low levels of turbulence the equilibrated flow with zonally symmetric mean forcing remains zonally symmetric, but as excitation increases it undergoes zonal symmetry-breaking bifurcations. Time-dependent flows arising from these bifurcations take the form of westward-propagating wavelike structures resembling blocking patterns. Features of these waves are characteristic of blocking in both observations and atmospheric general circulation model simulations including retrogression, eddy variance concentrated upstream of the waves, and eddy momentum flux forcing the waves.

1. Introduction

Obtaining a physical understanding of the low-frequency variability (LFV) of the midlatitude atmosphere at synoptic and planetary scales is a central problem in dynamic meteorology. A familiar manifestation of LFV is blocking (Dole and Gordon 1983; Dole 1986), in which the regional to planetary-scale flow deviates substantially from the climatological mean for time periods that can last several weeks producing anomalous temperatures and precipitation and results in disruption of agricultural activity and marked changes in power consumption (Carrera et al. 2004). Blocking frequently manifests as an amplification of the Pacific–North America (PNA) or North Atlantic Oscillation (NAO) patterns, and the magnitude of the PNA and NAO indices are strongly correlated with anomalies in temperature and precipitation associated with the patterns (Notaro et al. 2006). These strong correlations with regional climate provide additional motivation to understand the mechanisms underlying LFV.

Although atmospheric general circulation model (AGCMs) simulate the strength and location of the storm tracks, there is disagreement among them regarding LFV (D'Andrea et al. 1996). There are currently four prominent theories addressing the origin of LFV. The first identifies it as a weakly growing modal instability tied to zonal asymmetries in the background flow (Simmons et al. 1983; Swanson 2002). The second of these theories associates LFV with eddy–mean flow interactions (Shutts 1983; Robinson 1991). The third identifies LFV with attractors that resemble blocking patterns (Crommelin 2003), and the fourth identifies blocks with strongly nonlinear flow structures called modons (McWilliams 1980).

It has long been known that eddy interactions can force large-scale flows. Colucci (1985) presents a detailed case study showing propagation of a cyclone into a diffluence region triggering the onset of a blocking episode. Nakamura and Wallace (1990, 1993) show that transient eddy statistics are closely linked to the onset, maintenance, and decay of blocking patterns. In addition, observations show that eddy vorticity fluxes force planetary-scale flow in the midlatitudes (Holopainen

Corresponding author address: Joseph Bernstein, Dept. of Earth and Planetary Sciences, Harvard University, 20 Oxford St., Cambridge, MA 02138.
E-mail: jinmoon@gmail.com

DOI: 10.1175/2009JAS3170.1

© 2010 American Meteorological Society

et al. 1982; Holopainen and Fortelius 1987). These observational studies are compelling and are complemented by simulations using models of the atmosphere with simplified geometries demonstrating that turbulent fluxes play a crucial role in planetary-scale dynamics (Cai and Mak 1990; Robinson 1991; Branstator 1992). In addition to diagnostic studies, Shutts (1983) conducts an initial-value calculation in which waves propagate into a preexisting blocking pattern. The deformation of the eddies as they approach the block results in a vorticity flux enhancing the blocking pattern. The studies mentioned above establish that small-scale waves force large-scale flows. However, the interaction is not one way. Simulations also indicate that the large-scale flow organizes the smaller-scale transients and their associated fluxes (Cai and Mak 1990; Branstator 1995; Lorenz and Hartmann 2003), creating an inherently nonlinear problem in which the turbulence influences the large-scale flow, which in turn modifies the structure of the turbulence.

If we are to study this eddy–mean flow interaction it is necessary to use a method of analysis that incorporates this two-way interaction between the waves and mean flow. There are a number of theories in the literature describing both the turbulence and the eddy–mean flow interaction. The simplest idea available is eddy diffusivity of potential vorticity (PV). The main drawback of this method is that it fails to capture the upgradient momentum fluxes commonly observed in the midlatitude jet. Jin et al. (2006) propose a model describing the eddy–mean flow interactions that has success reproducing observed patterns. However, the climatological eddy variance in the model is fit to observations. The model we choose is stochastic structural stability theory (SSST; Farrell and Ioannou 2003), which captures the relevant turbulent fluxes without the use of data.

In SSST the turbulent eddy fluxes are obtained using a stochastic turbulence model (STM) (Farrell and Ioannou 1993a,b; DelSole 1996, 2004) that exploits the fact that in the nonlinear dynamics wave–wave interactions scatter energy, producing short time- and space-scale perturbations, while the nonnormality of the associated linear operator is responsible for the growth and structure of the perturbations and their associated fluxes. This allows construction of a model in which the scattering resulting from wave–wave nonlinearity is modeled as stochastic in space and time. One important feature of this model is its ability to reproduce both the cyclone response as well as a low wavenumber structure excited by the stochastic forcing (Farrell and Ioannou 1995). The low wavenumber response is commonly observed in the atmosphere and is sometimes brought up in the discussion of LFV (Whitaker and Barcilon 1995). However, in this work we model LFV as a large deviation that is not present in either the forced mean flow or the linear perturbation solution. To do this it is necessary to obtain the turbulent fluxes from the parameterization.

Previous studies show that the STM is in fact able to accurately reproduce the structure and spectra of midlatitude atmospheric eddies and their associated fluxes (Whitaker and Sardeshmukh 1998; Zhang and Held 1999). With the turbulent fluxes parameterized using the STM, a coupled set of eddy–mean flow equations can be derived for the coevolution of the mean flow and its consistent field of turbulent eddies. This SSST model has been studied in the context of a zonally averaged atmospheric jet (Farrell and Ioannou 2003). However, blocking is an inherently two-dimensional phenomena so that an intermediate time-scale mean rather than a zonal mean is appropriate for obtaining the eddy fluxes forcing the planetary-scale flow. In this work SSST is used to formulate the eddy–mean flow interaction in a two-dimensional channel with periodic boundaries using an intermediate time-scale mean separation between fast eddy and slow planetary-scale dynamics in an attempt to understand blocking in the atmosphere.

Section 2 contains a derivation of the coupled set of eddy–mean flow equations. Section 3 presents the results of the calculations. Section 4 compares these results with observations and AGCM studies. Section 5 contains the conclusions and discusses the future direction of this work.

2. Equations

A two-level baroclinic potential vorticity model with relaxation to a baroclinic equilibrium velocity structure is used (DelSole 1996). Our model differs from DelSole's model in the use of meridional sponge layers to enforce radiation boundary conditions and a scale-selective diffusion. The equations for the upper- and lower-level streamfunctions (ϕ_1 and ϕ_2) are written in terms of the barotropic and baroclinic streamfunction (ϕ_+ and ϕ_-)

$$\phi_+ \equiv \frac{1}{2}(\phi_1 + \phi_2) \quad \text{and}$$
$$\phi_- \equiv \frac{1}{2}(\phi_1 - \phi_2),$$

and the system is nondimensionalized using typical mean zonal velocity and synoptic space scales $U = 30$ m s^{-1} and $L = 2820$ km, giving $T = LU^{-1} \approx 1$ day. The resulting nondimensional equations are

$$(\nabla_f^2)\frac{\partial \phi_-}{\partial t} = J(\nabla_f^2\phi_-, \phi_+) + J(\nabla^2\phi_+, \phi_-) - \beta\frac{\partial \phi_-}{\partial x} - r\nabla^2(\phi_-) - \frac{\partial r}{\partial y}\frac{\partial \phi_-}{\partial y} + A\nabla^4\phi_- - r_e(\phi_- - \Theta_e) \quad \text{and} \tag{1}$$

$$(\nabla^2)\frac{\partial \phi_+}{\partial t} = J(\nabla^2\phi_+, \phi_+) + J(\nabla^2\phi_-, \phi_-) - \beta\frac{\partial \phi_+}{\partial x} - r\nabla^2(\phi_+) - \frac{\partial r}{\partial y}\frac{\partial \phi_+}{\partial y} + A\nabla^4\phi_+, \tag{2}$$

where

$$J(\kappa, \lambda) = \frac{\partial \kappa}{\partial x}\frac{\partial \lambda}{\partial y} - \frac{\partial \kappa}{\partial y}\frac{\partial \lambda}{\partial x},$$
$$\nabla_f^2\kappa = \frac{\partial^2 \kappa}{\partial x^2} + \frac{\partial^2 \kappa}{\partial y^2} - \mathrm{Fr}\kappa,$$

and the sponge layer is defined as

$$r = r_{\mathrm{sp}}2\left[2 + \tanh\left(\frac{y - 1.7}{0.1}\right) - \tanh\left(\frac{y - 0.3}{0.1}\right)\right].$$

A dimensional value of $\beta_{\mathrm{dim}} = 1.6e - 11\ \mathrm{s}^{-1}\ \mathrm{m}^{-1}$ is nondimensionalized using $\beta = \beta_{\mathrm{dim}}L^2U^{-1}$. The dimensionless parameters are $\beta = 4.3$, Froude number $\mathrm{Fr} = 1$, radiative damping rate $r_e = 0.05$, diffusion constant $A = 0.02$, and the magnitude of the sponge layer damping rate $r_{\mathrm{sp}} = 0.1$. The boundary conditions are periodic in the zonal direction and rigid channel walls with sponge layers enforcing a radiation condition in the meridional. The channel extent is $2L$ in both zonal and meridional directions.

a. Equation for the fast variables

Splitting the baroclinic and barotropic streamfunctions into an intermediate time mean (assumed to be approximately 3–4 days) and the deviation from this mean gives

$$\phi_+ \equiv \Psi + \psi$$
$$\phi_- \equiv \Theta + \theta.$$

Subtracting the equations for evolution of the intermediate time-scale variables from (1) and (2), we obtain an evolution equation for perturbations (ψ and θ):

$$\partial_t(\nabla^2\psi) = N_\psi + \pounds\psi \quad \text{and} \quad \partial_t(\nabla_f^2\theta) = N_\theta + \pounds\theta, \tag{3}$$

where

$$\pounds = -\beta\frac{\partial}{\partial x} + A\nabla^4 - r(y)\nabla^2 - \frac{\partial r}{\partial y}\frac{\partial}{\partial y},$$

$$N_\psi = N_{\theta\theta} + N_{\psi\psi} + J(\nabla^2\psi, \psi) + J(\nabla^2\theta, \theta), \quad \text{and}$$
$$N_\theta = N_{\psi\theta} + N_{\theta\psi} + J(\nabla_f^2\theta, \psi) + J(\nabla^2\psi, \theta);$$

and

$$N_{\theta\theta} = J(\nabla^2\Theta, \theta) + J(\nabla^2\theta, \Theta),$$
$$N_{\psi\psi} = J(\nabla^2\Psi, \psi) + J(\nabla^2\psi, \Psi),$$
$$N_{\theta\psi} = J(\nabla_f^2\theta, \Psi) + J(\nabla_f^2\Theta, \psi), \quad \text{and}$$
$$N_{\psi\theta} = J(\nabla^2\Psi, \theta) + J(\nabla^2\psi, \Theta).$$

The terms N_θ and N_ψ are made up of four nonlinear terms mixing the intermediate time-scale variables, which we will call slow, and the deviations, which we refer to as fast (double subscript) and two nonlinear terms involving only fast time scales each. These fast–fast nonlinear terms are approximated by a stochastic excitation with a specified spatial structure. DelSole (1996) uses a linear inverse model of a geostrophically turbulent system to show that the linear Markov model just described can be used to adequately approximate the turbulence. With this in mind, let $\eta(t)$ be a zero mean unit variance (white) noise process, $\mathcal{F}$ be a spatial structure, and ε the magnitude of the stochastic excitation. This approximation transforms (3) into a coupled set of linear stochastic differential equations that can be written as

$$\frac{\partial}{\partial t}\begin{bmatrix}\psi\\ \theta\end{bmatrix} = \mathcal{A}\begin{bmatrix}\psi\\ \theta\end{bmatrix} + \epsilon^{1/2}\mathcal{F}\begin{bmatrix}\eta_\psi\\ \eta_\theta\end{bmatrix}, \tag{4}$$

with

$$\mathcal{A} \equiv \begin{bmatrix}\nabla^2 & 0\\ 0 & \nabla_f^2\end{bmatrix}^{-1}\left(\begin{bmatrix}N_{\psi\psi} & N_{\psi\theta}\\ N_{\theta\psi} & N_{\theta\theta}\end{bmatrix} + \begin{bmatrix}\pounds & 0\\ 0 & \pounds\end{bmatrix}\right),$$

where square brackets indicate a matrix. The operators discussed thus far have been continuous. However, all calculations must be done using discrete approximations. Second-order accurate finite difference operators on a uniform grid are used to represent all derivatives. Let the discretized linear operator representing $\mathcal{A}$ be $\mathbf{A}$, the discretized forcing structure $\mathcal{F}$ be $\mathbf{F}$, the discretized state vector be $\mathbf{p}$, the discretized noise vector be $\mathbf{n}(t)$, and the infinite ensemble average covariance matrix be $\mathbf{C} = \langle\mathbf{p}\mathbf{p}^{\mathrm{T}}\rangle$, where angle brackets denote ensemble averaging. The ensemble average is over an infinite number of realizations of $\mathbf{p}$, whose structure depends on the particular realization of the noise $\mathbf{n}(t)$. This transforms (4) into

$$\frac{\partial \mathbf{p}}{\partial t} = \mathbf{A}\mathbf{p} + \epsilon^{1/2}\mathbf{F}\mathbf{n}(t).$$

The infinite ensemble covariance matrix $\mathbf{C}$ associated with (4) evolves in time according to the time-dependent Lyapunov equation

$$\frac{\partial \mathbf{C}}{\partial t} = \mathbf{AC} + \mathbf{CA}^{\mathrm{T}} + \varepsilon \mathbf{Q}, \tag{5}$$

where $\mathbf{Q} = \mathbf{FF}^{\mathrm{T}}$ and the magnitude of the excitation is controlled by ε. For convenience the excitation structure ($\mathbf{Q}$) is scaled so that $\varepsilon = 1$ corresponds to an earth-equivalent energy injection rate of 1 W m^{-2} (see appendix). Realistic estimates for the actual energy injection rate are on the order of 1 W m^{-2} according to DelSole and Farrell (1995) and Farrell and Ioannou (1994), and an energy injection rate of 1.3 W m^{-2} in our model produces an eddy meridional velocity variance of approximately 700 m^2 s^2, which is in agreement with observations of midwinter Northern Hemisphere values in the Atlantic (Chang et al. 2002).

It is crucial to note that the Lyapunov Eq. (5) is autonomous and deterministic. The eddy fluxes are easily found from the covariance matrix $\mathbf{C}$, meaning that although the eddy parameterization is stochastic in nature, the eddy–mean flow interaction is captured by this coupled set of deterministic autonomous differential equations, which provides the theoretical formulation with both clarity and simplicity. It remains to derive the time-dependent mean flow equation for the evolution of the slow variable.

b. Equation for the slow variable

If the change in the basic-state variable occurs slowly compared to eddy life cycles, then an intermediate time scale can be identified for which

$$\overline{\psi} = \overline{\theta} = 0$$

and

$$\overline{\Psi} = \overline{\Psi}, \quad \overline{\Theta} = \overline{\Theta}.$$

This is the method of Reynolds averaging (Holton 1992), and in this work its main function is to eliminate terms that contain both a slow and fast variable in the expression for the evolution of the slow variable while retaining the fast–fast interaction term that has been parameterized above. Studies show that the fast–fast fluxes are the dominant terms in the forcing of the mean flow (Robinson 1991) and this assumption, although idealized, reduces the slow variable equation to a relaxation to a radiative-equilibrium temperature gradient, the β effect, mean flow advection, and a heat and vorticity flux due to the fast variables:

$$(\nabla_f^2)\frac{\partial \Theta}{\partial t} = \overline{J(\nabla_f^2\theta, \psi)} + \overline{J(\nabla^2\psi, \theta)} - \beta\frac{\partial \Theta}{\partial x} - r_e(\Theta - \Theta_e) + J(\nabla_f^2\Theta, \Psi) + J(\nabla^2\Psi, \Theta), \quad \text{and} \tag{6}$$

$$(\nabla^2)\frac{\partial \Psi}{\partial t} = \overline{J(\nabla^2\psi, \psi)} + \overline{J(\nabla^2\theta, \theta)} - \beta\frac{\partial \psi}{\partial x} + J(\nabla^2\Psi, \Psi) + J(\nabla^2\Theta, \Theta), \tag{7}$$

where the overbar represents a time average over the intermediate scale just discussed. To couple the perturbation and mean flow equations we write the fluxes in terms of the fast variable covariance $\mathbf{C}$. To simplify this task we split $\mathbf{C}$ into four parts:

$$\mathbf{C} = \begin{bmatrix} \mathbf{C}_{\psi\psi} & \mathbf{C}_{\psi\theta} \\ \mathbf{C}_{\theta\psi} & \mathbf{C}_{\theta\theta} \end{bmatrix} = \begin{bmatrix} \langle \psi\psi^{\mathrm{T}} \rangle & \langle \psi\theta^{\mathrm{T}} \rangle \\ \langle \theta\psi^{\mathrm{T}} \rangle & \langle \theta\theta^{\mathrm{T}} \rangle \end{bmatrix}.$$

Choosing one of the heat flux terms and writing out the Jacobian gives

$$\begin{aligned} \overline{J(\nabla^2\theta, \psi)} &= \overline{\left(\frac{\partial}{\partial x}\nabla^2\theta\right)\left(\frac{\partial \psi}{\partial y}\right) - \left(\frac{\partial}{\partial y}\nabla^2\theta\right)\left(\frac{\partial \psi}{\partial x}\right)} \\ &= \frac{\partial}{\partial x}\overline{\left(\frac{\partial \psi}{\partial y}\nabla^2\theta\right)} - \frac{\partial}{\partial y}\overline{\left(\frac{\partial \psi}{\partial x}\nabla^2\theta\right)}. \end{aligned}$$

If we write the continuous operators in terms of their discretized counterparts,

$$\frac{\partial}{\partial x} \to \mathbf{D}_x, \quad \frac{\partial}{\partial y} \to \mathbf{D}_y,$$

$$\nabla^2 \to \mathbf{D}_2, \quad \psi \to \mathbf{p}, \quad \text{and} \quad \theta \to \mathbf{h},$$

then the flux term becomes

$$J(\nabla^2\theta, \psi) = \mathbf{D}_x\,\overline{\mathrm{diag}(\mathbf{D}_y\mathbf{p}\mathbf{h}^{\mathrm{T}}\mathbf{D}_2^{\mathrm{T}})} - \mathbf{D}_y\,\overline{\mathrm{diag}(\mathbf{D}_x\mathbf{h}\mathbf{p}^{\mathrm{T}}\mathbf{D}_2^{\mathrm{T}})}.$$

Finally, if we make the assumption that the slow time mean is equivalent to the ensemble mean, then

$$\overline{J(\nabla^2\theta, \psi)} = \mathbf{D}_x\,\mathrm{diag}(\mathbf{D}_y\mathbf{C}_{\psi\theta}\mathbf{D}_2^{\mathrm{T}}) - \mathbf{D}_y\,\mathrm{diag}(\mathbf{D}_x\mathbf{C}_{\theta\psi}\mathbf{D}_2^{\mathrm{T}}).$$

The rest of the fluxes can be written similarly:

$$\overline{J(\nabla^2\psi, \theta)} = \mathbf{D}_x\,\mathrm{diag}(\mathbf{D}_y\mathbf{C}_{\theta\psi}\mathbf{D}_2^{\mathrm{T}}) - \mathbf{D}_y\,\mathrm{diag}(\mathbf{D}_x\mathbf{C}_{\theta\psi}\mathbf{D}_2^{\mathrm{T}}),$$

$$\overline{J(\nabla^2\psi, \psi)} = \mathbf{D}_x\,\mathrm{diag}(\mathbf{D}_y\mathbf{C}_{\psi\psi}\mathbf{D}_2^{\mathrm{T}}) - \mathbf{D}_y\,\mathrm{diag}(\mathbf{D}_x\mathbf{C}_{\psi\psi}\mathbf{D}_2^{\mathrm{T}}), \quad \text{and}$$

$$\overline{J(\nabla^2\theta, \theta)} = \mathbf{D}_x\,\mathrm{diag}(\mathbf{D}_y\mathbf{C}_{\theta\theta}\mathbf{D}_2^{\mathrm{T}}) - \mathbf{D}_y\,\mathrm{diag}(\mathbf{D}_x\mathbf{C}_{\theta\theta}\mathbf{D}_2^{\mathrm{T}}).$$

Now the mean flow in (6) and (7) is forced by the eddy covariances **C**, which evolve according to the time-dependent Lyapunov Eq. (5).

We make a brief aside here to discuss the nature of Reynolds averaging and its impact on the dynamics. The initial averaging is in the time domain. An intermediate time scale is chosen that is short compared to the time scale for the evolution of the mean flow but long compared to the eddy time scale. This intermediate time average is then replaced by an ensemble average, the reasoning being that over this intermediate time scale a number of eddies will pass by, acting as independent members of the ensemble. Realistically, this ensemble average occurs over a finite number of eddies because the time interval averaged over is finite. To obtain the Lyapunov equation we need to make the additional assumption that this finite ensemble mean is well approximated by the infinite ensemble mean. The finite ensemble mean converges to the infinite ensemble average with an error of $O(n^{-1/2})$ for n members. However, in the atmosphere we are averaging over a small number of realizations so we expect the actual turbulent system to display irregular behavior. Nonetheless, it is instructive to examine the ensemble mean set of equations and the structures they generate.

c. Free parameters

The first free parameter in our model is the radiative-equilibrium thermal forcing,

$$\Theta_e = -\frac{1}{2}\left\{ Y + \frac{1}{\pi} \sin[\pi(Y-1)] \right\}, \tag{8}$$

which tends to produce a thermal wind–balanced zonal baroclinic jet (Fig. 1). The next free parameter is the **Q** matrix. The choice of **Q** controls the spatial structure of the noise. In extreme cases, if chosen unwisely, it can produce unphysical results. A spatially uniform excitation excites waves both inside and outside of the jet and these waves radiate momentum both into and out of the jet. If damping is small, the flux from the waves outside the jet can dominate the momentum flux, providing downgradient fluxes damping the jet. In our examples the diagonal of **F** is set to Θ_e so that the excitation is confined to the region of the jet. The off-diagonal elements of **F** are set to zero, indicating a spatially uncorrelated excitation.

The inherently nonlinear nature of our model invites the use of methods from bifurcation theory to understand the dynamics (Guckenheimer and Holmes 1983). The strength of the excitation ε is used as the bifurcation parameter for the problem. The model is now completely specified. It is nonlinear, deterministic, and autonomous in spite of the underlying stochastic nature of the parameterizations. The next section presents the bifurcation structure of the coupled equilibria calculations.

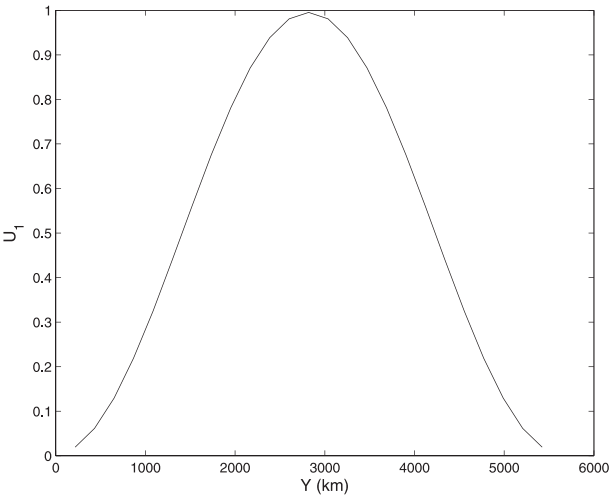

FIG. 1. Radiative-equilibrium upper-level jet velocity. Lower-layer jet relaxes to zero.

3. Results

A 25×25 grid is used, giving a resolution of approximately 225 km in both directions. These $N = 25$ grid points in each direction gives a total of $O(N^2)$ points for the system and $O(N^4)$ points for the covariance matrix. If the Jacobian were to be approximated using finite difference methods in order to employ a descent algorithm to find the equilibrium, this would require $O(N^2)$ solutions of the Lyapunov Eq. (5), which becomes prohibitively expensive. An alternative method is to numerically integrate the coupled equations in time. Although the structure of unstable solutions cannot be found directly using this method, it is efficient enough to explore the bifurcation structure for a wide range of ε. A fourth-order Runge–Kutta time stepping scheme is used because of its accuracy and stability properties.

To compare our calculations with previous studies we obtain the structure of the turbulence in equilibrium with a fixed flow. This is done by solving the Lyapunov Eq. (5) using Θ_e as the background flow. The spectra of the empirical orthogonal functions (EOFs) and the stochastic optimals (Farrell and Ioannou 1996) are shown in Figs. 2a,b. Both spectra show two modes well separated from the rest of the spectrum. These modes are phase-shifted versions of the same structure. Two modes exist because there is a single propagating structure. The upper- and lower-layer streamfunctions for the leading EOF and stochastic optimal are plotted in Figs. 2c–f. The leading

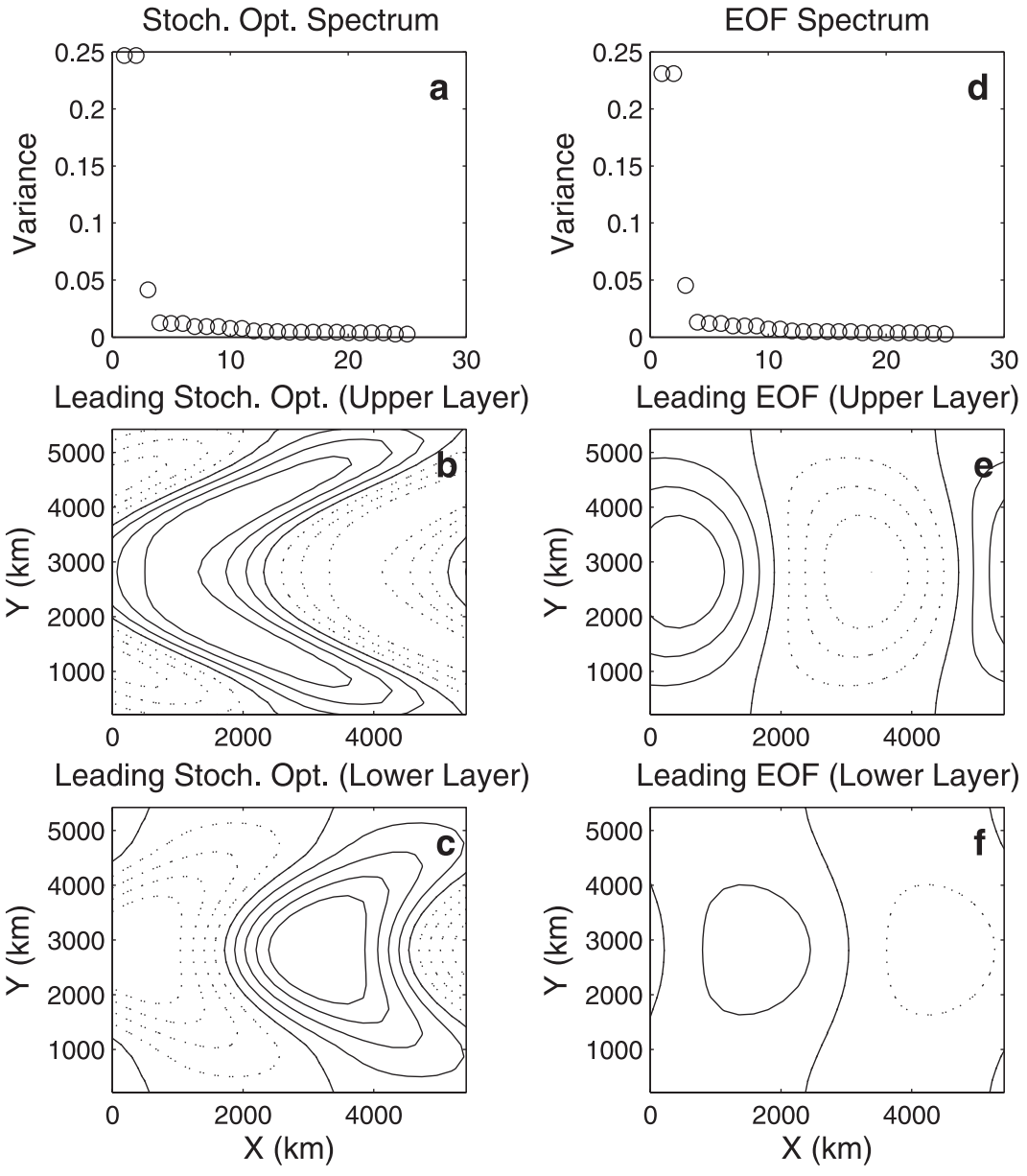

FIG. 2. Structure of the turbulence for the radiative-equilibrium jet. Solid contours are positive and dotted contours are negative. (a),(d) Spectra for the first 25 EOFs and stochastic optimals, respectively. (b) Upper- and (c) lower-layer streamfunction for the leading optimal with contour intervals 1.3×10^6 m^2 s^{-1}. (e) Upper- and (f) lower-layer streamfunction for the leading EOF with contour intervals 2.4×10^6 m^2 s^{-1}.

stochastic optimal has a phase-shifted vertical structure so that it is leaning against the imposed vertical shear extracting mean baroclinic energy. The meridional structure of the optimal is tilted against the meridional shear on each side of the jet maximum extracting mean barotropic energy as well. The lower-layer structure has less meridional tilt consistent with there being no lower-layer flow to extract energy from. The leading EOF is approximately equivalent-barotropic with a small vertical tilt against the shear, indicative of positive mean baroclinic energetics acting to reduce the mean temperature gradient. The meridional structure of the EOF tilts with the shear, indicative of negative mean barotropic energetics maintaining the barotropic jet. We now calculate the equilibrium structures that the eddy–mean flow interactions produce.

a. Stable fixed points

The initial structure of the turbulence and associated fluxes was discussed in the previous section. These fluxes

create a nonzero Θ_t and Ψ_t so that the mean flow evolves in time. The radiative equilibrium shown in Fig. 1, corresponding to $\varepsilon = 0$, is zonally homogenous, consisting of a jet in the upper layer and zero flow in the lower layer. For nonzero ε the system initially remains zonally homogenous and equilibrates to a stable fixed point. Therefore, only zonally averaged quantities are presented in Fig. 3, which summarizes the properties of the equilibria. The zonally averaged stable fixed points are shown for a small energy injection rate $\varepsilon = 0.5$ and an energy injection rate of 1.5, which reproduces observed eddy variance. The radiative-equilibrium flow is plotted for comparison. The lower-layer flow is initially zero, but the fluxes drive a lower-layer jet with a positive velocity in the center and negative velocities toward the flanks. The equilibrated upper-layer flow has a smaller maximum velocity than the radiative equilibrium. This becomes more pronounced as ε increases.

Comparison to the equilibration of jets in eddy-resolving models is difficult because of the myriad of configurations available for simulations. Our model is based on DelSole (1996) and the equilibration resembles his results (see his Fig. 1). Whitaker and Barcilon (1995) run a similar model with a different formulation of dissipation and a weaker mean flow. Their equilibration shows a stronger upper-level jet as well as the formation of multiple jets. These cases illustrate the difficulty in comparing models unless the parameter setting is similar. Although our particular model does not show multiple jets, the SSST formulation is capable of producing multiple jets in other cases (Farrell and Ioannou 2007, 2008).

b. Limit cycles

1) CONSTANT DIPOLE BLOCKING STRUCTURE

For $\varepsilon = \varepsilon_c \approx 2.3$ the system undergoes a bifurcation and enters into a limit cycle as shown in Fig. 4. We refer to this structure as a constant block. It is important to note that even though we refer to this structure as a block, there is no onset or decay associated with the structure. The limit cycle consists of a westward-propagating wave whose spatial structure is constant. The upper-layer flow is still westerly, but it now has a wave structure with zonal wavenumber ($k = 1$) and meridional wavenumber ($l = 2$). The structure consists of a confluence and diffluence region (Fig. 4a) and closely resembles the classic dipole blocking pattern with a zonal jet. The structure in the lower layer is the same except the velocities are an order of magnitude smaller and the flanks of the jet flow westward (not shown). The spatial structure remains meridionally symmetric, but the zonal symmetry is broken. The entire structure propagates westward

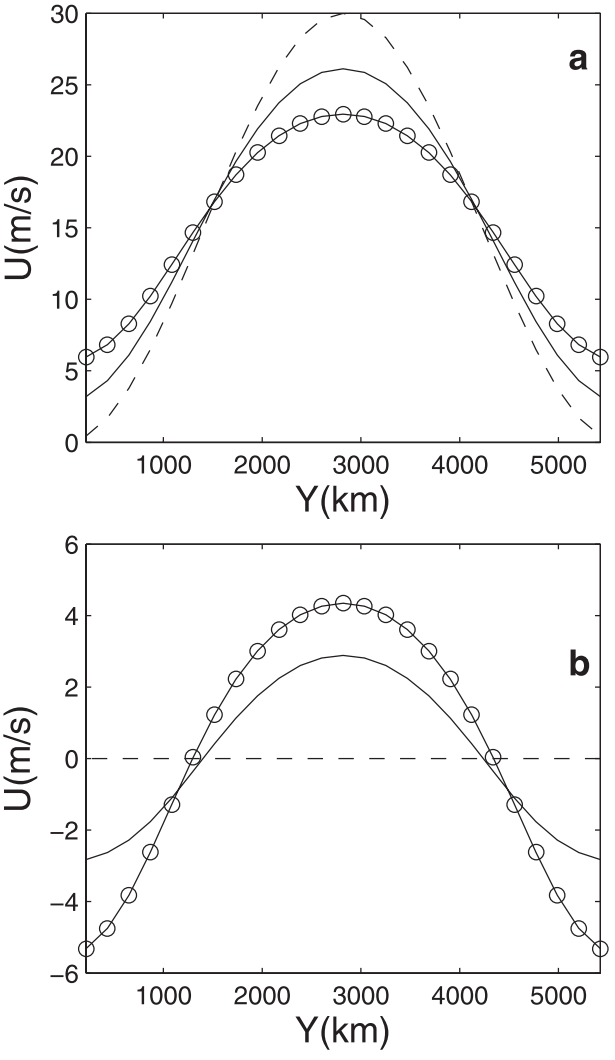

FIG. 3. Turbulent equilibria, which are stable fixed points, are shown for several values of excitation (ε). (a) Zonally averaged upper-layer zonal velocity. (b) Zonally averaged lower-layer zonal velocity. The dashed line indicates the radiative-equilibrium velocity, the solid line indicates $\varepsilon = 0.5$, and the solid line with circles indicates $\varepsilon = 1.5$.

extremely slowly with phase speed $O(0.06)$ m s^{-1}. By defining

$$F_{\mathrm{bc}} = \nabla_f^{-1}[\overline{J(\nabla_f^2\theta, \psi)} + \overline{J(\nabla\psi, \theta)}],$$

$$F_{\mathrm{bt}} = \nabla_f^{-1}[\overline{J(\nabla^2\psi, \psi)} + \overline{J(\nabla^2\theta, \theta)}],$$

and referring to (6) and (7), we see that these are the turbulent forcing terms for the baroclinic and barotropic components of the flow, respectively. Adding them together gives the turbulent forcing of the upper layer, which is shown in Fig. 4b. The contributions to the total streamfunction tendency budget by mean flow advection,

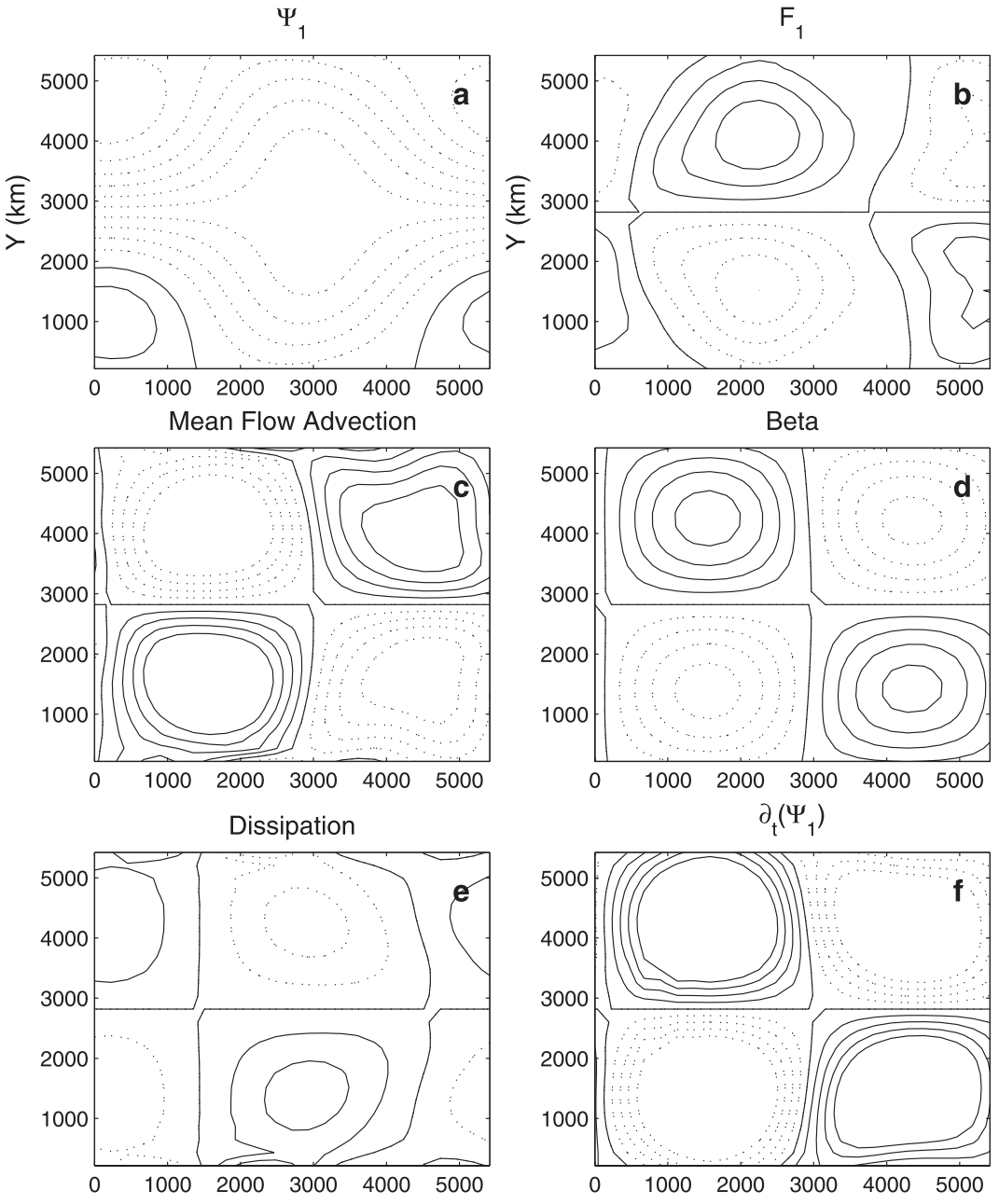

FIG. 4. Diagnostics of the eddy–mean flow interaction just after the system enters into a limit cycle at $\varepsilon_c = 2.5$. (a) Snapshot of upper-layer streamfunction with contour interval 1×10^8 m^2 s^{-1}. (b)–(e) Streamfunction tendency (b) induced by turbulence in the upper layer, (c) due to mean flow advection in the upper layer, (d) due to β effect in the upper layer, and (e) due to dissipation and thermal forcing, all with contour interval $0.35 \times$ m^2 s^{-2}; (f) total streamfunction tendency in the upper layer, with contour interval 0.35×10^{-2} m^2 s^{-2}.

β effect, dissipation, and thermal forcing are shown in Figs. 4c, 4d, and 4e, respectively. The total streamfunction tendency is shown in Fig. 4f and is almost two orders of magnitude smaller then the individual components, indicating a large degree of cancelation among the terms. According to Fig. 4 the turbulent forcing and β effect tend to produce retrogression whereas the mean flow advection tendency is prograde, creating a three-way balance. Dissipation and thermal forcing play a small role in the dynamical balance. The total streamfunction tendency is weak, producing the slow net retrograde motion. Additional dynamical aspects of the flow are shown in Fig. 5. The upper-layer eddy variance is calculated using

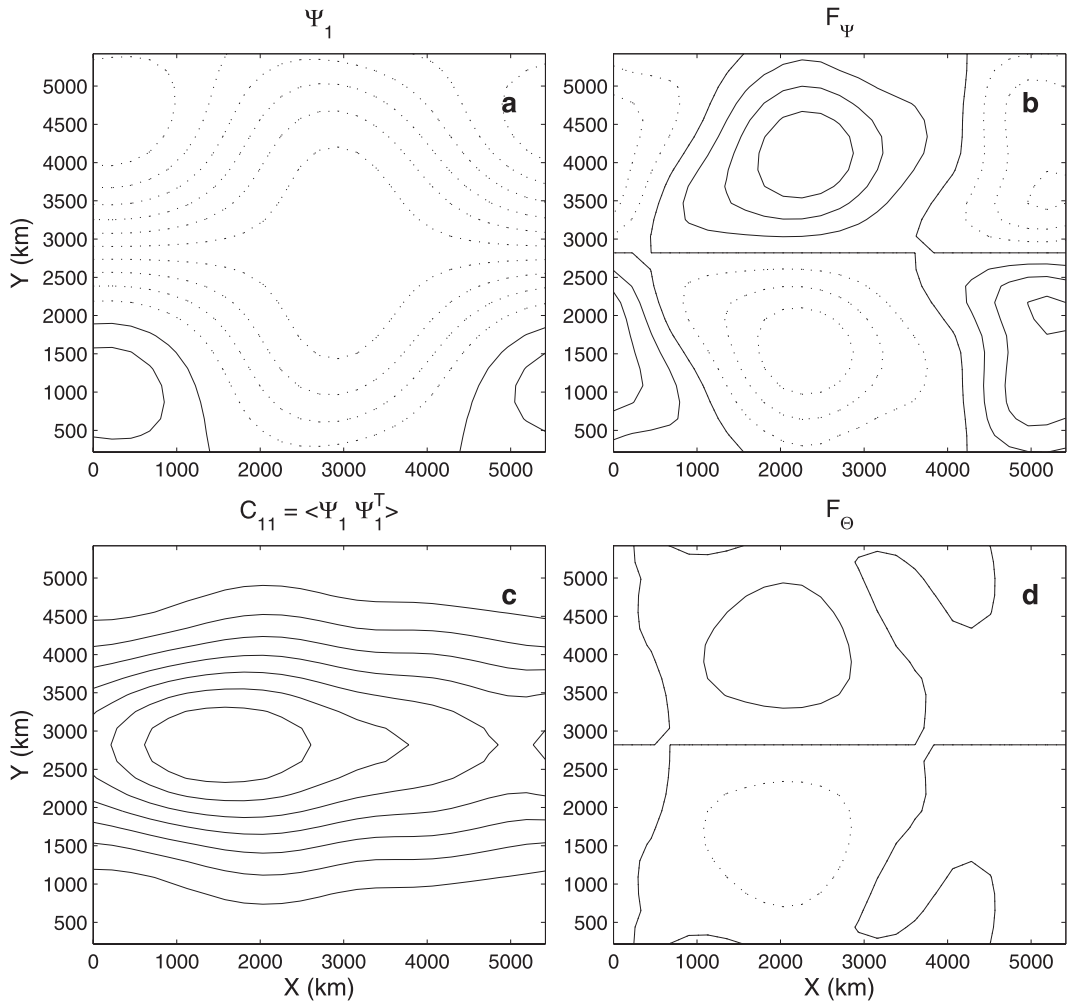

FIG. 5. Diagnostics of the eddy–mean flow interaction after the system enters into a limit cycle at $\varepsilon_c = 2.5$. (a) Snapshot of upper-layer streamfunction with contour interval 1×10^8 m^2 s^{-1}. (b) Barotropic component of the streamfunction tendency induced by turbulence with contour interval 25 m^2 s^{-2}. (c) Upper-layer eddy variance with contour interval 20 m^4 s^{-2}. (d) Baroclinic component of the streamfunction tendency due to the β effect in the upper layer with contour interval 0.35 m^2 s^{-2}.

$$\begin{aligned}\mathbf{C_{11}} &= \langle \phi_1' \phi_1'^{\mathrm{T}} \rangle = \langle (\psi + \theta)(\psi + \theta)^{\mathrm{T}} \rangle \\ &= \langle \psi\psi^{\mathrm{T}} \rangle + \langle \theta\psi^{\mathrm{T}} \rangle + \langle \psi\theta^{\mathrm{T}} \rangle + \langle \theta\theta^{\mathrm{T}} \rangle \\ &= \mathbf{C}_{\psi\psi} + \mathbf{C}_{\theta\psi} + \mathbf{C}_{\psi\theta} + \mathbf{C}_{\theta\theta}\end{aligned}$$

and is plotted below $\overline{\phi}_1$ for reference. The maximum is located in the downstream region of the zonal jet. The turbulent fluxes in terms of their barotropic and baroclinic components are shown in Figs. 5c,d. It is evident that both heat and vorticity fluxes support the blocking patterns, although the barotropic component is noticeably stronger. The fluxes are strongest in the jet exit because this is the area of greatest deformation and the deformation of eddies produces momentum fluxes, amplifying the block (Shutts 1983).

The frequency of the wave as a function of ε is shown in Fig. 6. Close to ε_c the frequency of the wave is almost zero and as ε increases the frequency grows linearly with ε. The amplitude of the limit cycle can be measured by the $L2$ norm of the deviation from radiative equilibrium of the upper and lower streamfunction:

$$N_a = \sum_{i=1}^{N}\sum_{j=1}^{N} ([\Psi_{ij} - (\Psi_e)_{ij}]^2 + [\Theta_{ij} - (\Theta_e)_{ij}]^2).$$

For $\varepsilon < \varepsilon_c$ the flow is zonally symmetric and for $\varepsilon > \varepsilon_c$ a finite-amplitude wave appears. The amplitude of this wave increases linearly with ε as shown in Fig. 6. The amplitude of the wave grows because increasing ε correspondingly increases the turbulent forcing, which supports

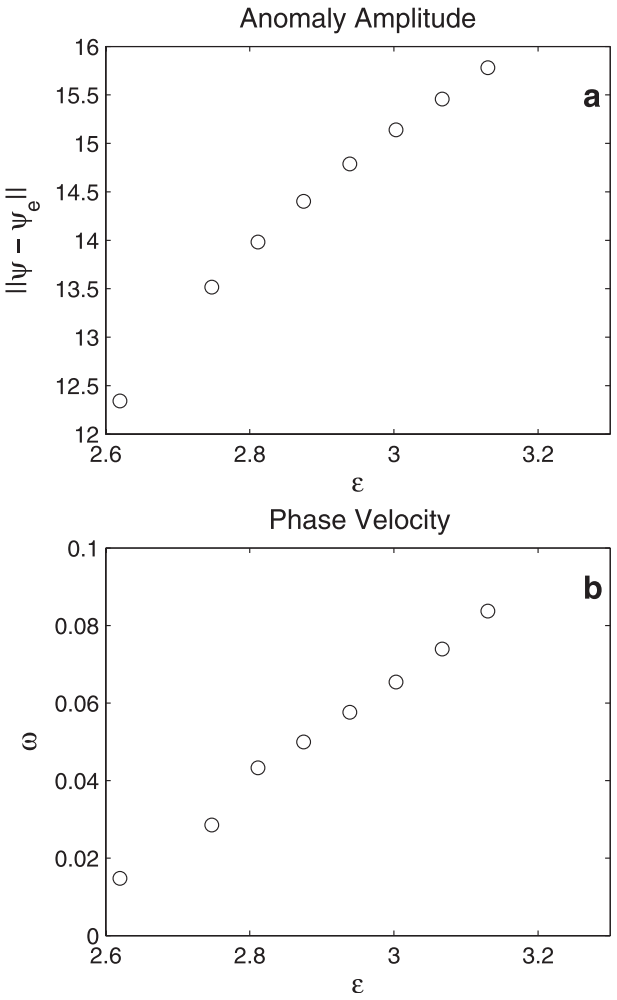

FIG. 6. Dependence of the limit cycle on excitation ε: (a) amplitude of the zonal anomaly and (b) propagation velocity.

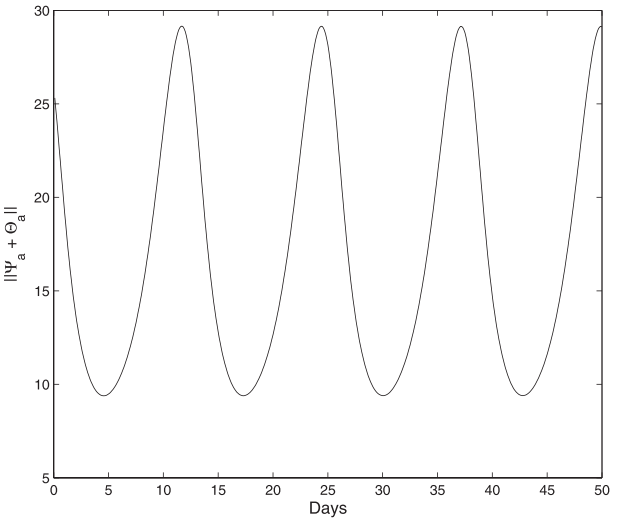

FIG. 7. Block oscillation indicated by the L2 norm of the deviation from radiative equilibrium of the upper- and lower-layer streamfunction as a function of time after the second bifurcation at $\varepsilon = 3.5$. The changing amplitude of N_a shows that the time-dependent behavior is no longer confined to retrograde propagation but extends into the spatial structure of the block. To understand the oscillation in the spatial structure, we analyze the flow at maximum and minimum N_a.

the wave. The growth of the phase speed is due to the increase in amplitude because as the amplitude of the block grows, the deformation region in the jet exit becomes stronger; this results in the eddy variance becoming increasingly concentrated upstream of the block because the deformation prevents propagation of eddies into the block. This localizes the fluxes farther upstream and the further upstream of the block the forcing occurs, the more rapidly it propagates. For $\varepsilon = 3.3$ the system undergoes another bifurcation.

2) OSCILLATING BLOCK

This limit cycle is referred to as the oscillating block. The period and amplitude of the limit cycle measured using N_a are shown in Fig. 7 for $\varepsilon = 3.5$. The variation of N_a shown in Fig. 7 shows that the block time dependence is no longer confined to retrograde propagation but extends to the spatial structure of the block. To better characterize this oscillation in spatial structure we examine the flow at maximum and minimum N_a. The period of the limit cycle is 12 days and the spatial structure at the maxima and minima of the oscillation are shown in Figs. 8 and 9, respectively. The upper-layer streamfunction when N_a is at a minimum is a weak block. The eddy variance is located near the center of the block (Fig. 9b) and the streamfunction tendency is in phase with the zonal dipole anomaly (Fig. 9). This causes the dipole pattern to grow without propagation. This growth occurs until N_a reaches a maximum. Now the upper-layer streamfunction consists of a strong blocking dipole (Fig. 8a) and the eddy variance is located upstream of the block in the diffluence region of the flow (Fig. 8a). It is stronger and more localized than at the minimum of N_a. In addition, the streamfunction tendency has shifted upstream and is out of phase with the block (Fig. 8e). This results in upstream propagation of the whole structure. As the block propagates upstream it weakens because the streamfunction tendency is no longer in phase with the block. The weakening of the block results in the zonal elongation and reduction in magnitude of the eddy variance. This continues until the eddy variance is situated inside the block, at which point the streamfunction tendency is in phase with the block and it grows again.

The properties of the limit cycle as a function of ε are shown in Fig. 10. The amplitude of the limit cycle grows with ε but begins to saturate for large ε because it is

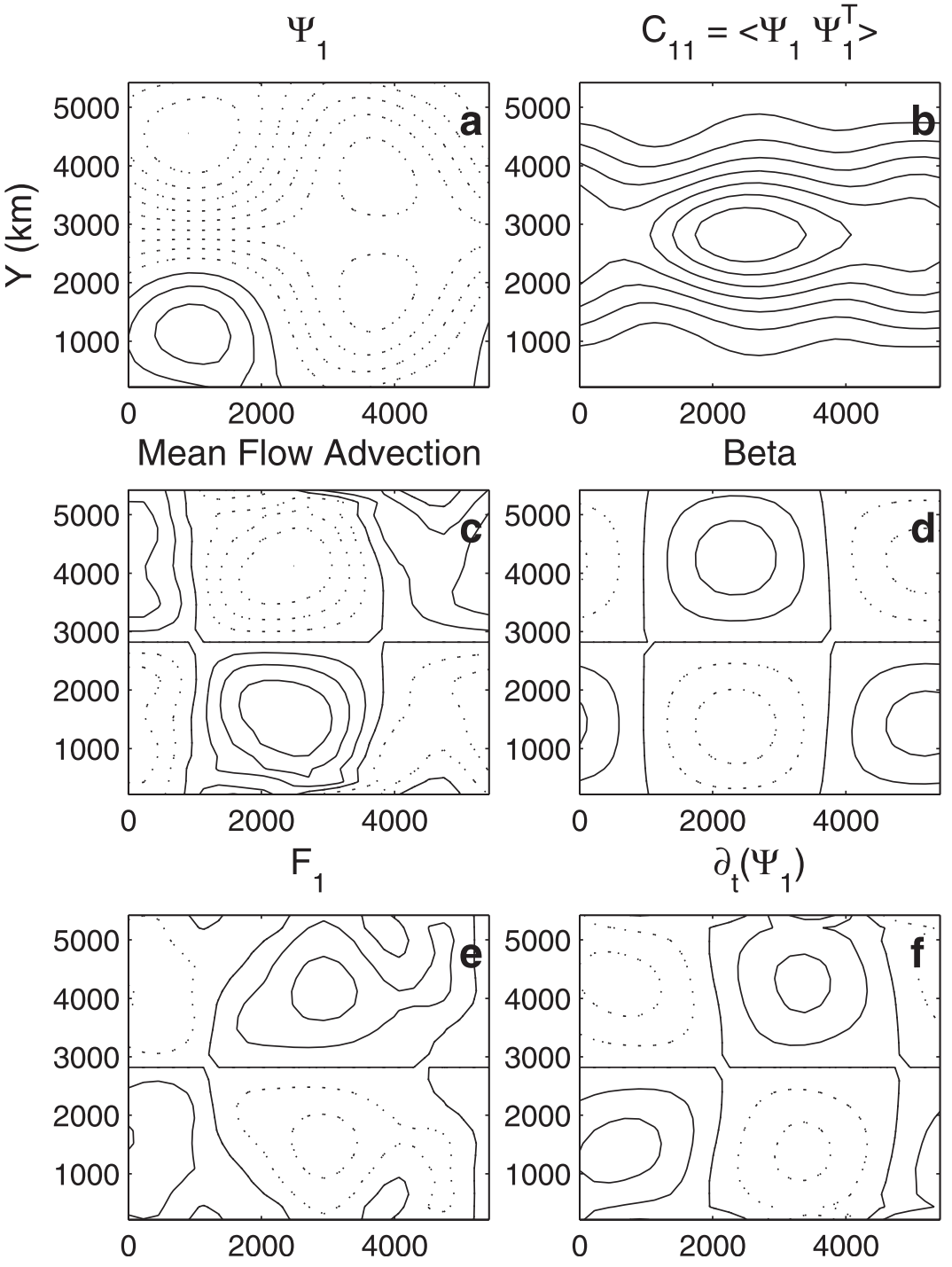

FIG. 8. Diagnostics of the maximum norm case for the second limit cycle at $\varepsilon = 3.5$. (a) Snapshot of upper-layer streamfunction with contour interval 1.2×10^8 m^2 s^{-1}. (b) Upper-layer eddy variance with contour interval 42 m^4 s^{-2}. (c) Streamfunction tendency due to mean flow advection in the upper layer with contour interval 2 m^2 s^{-2}. (d) Streamfunction tendency due to the β effect in the upper layer with contour interval 2 m^2 s^{-2}. (e) Streamfunction tendency induced by turbulence in the upper layer with contour interval 2 m^2 s^{-2}. (f) Total streamfunction tendency in the upper layer with contour interval 2×10^{-2} m^2 s^{-2}.

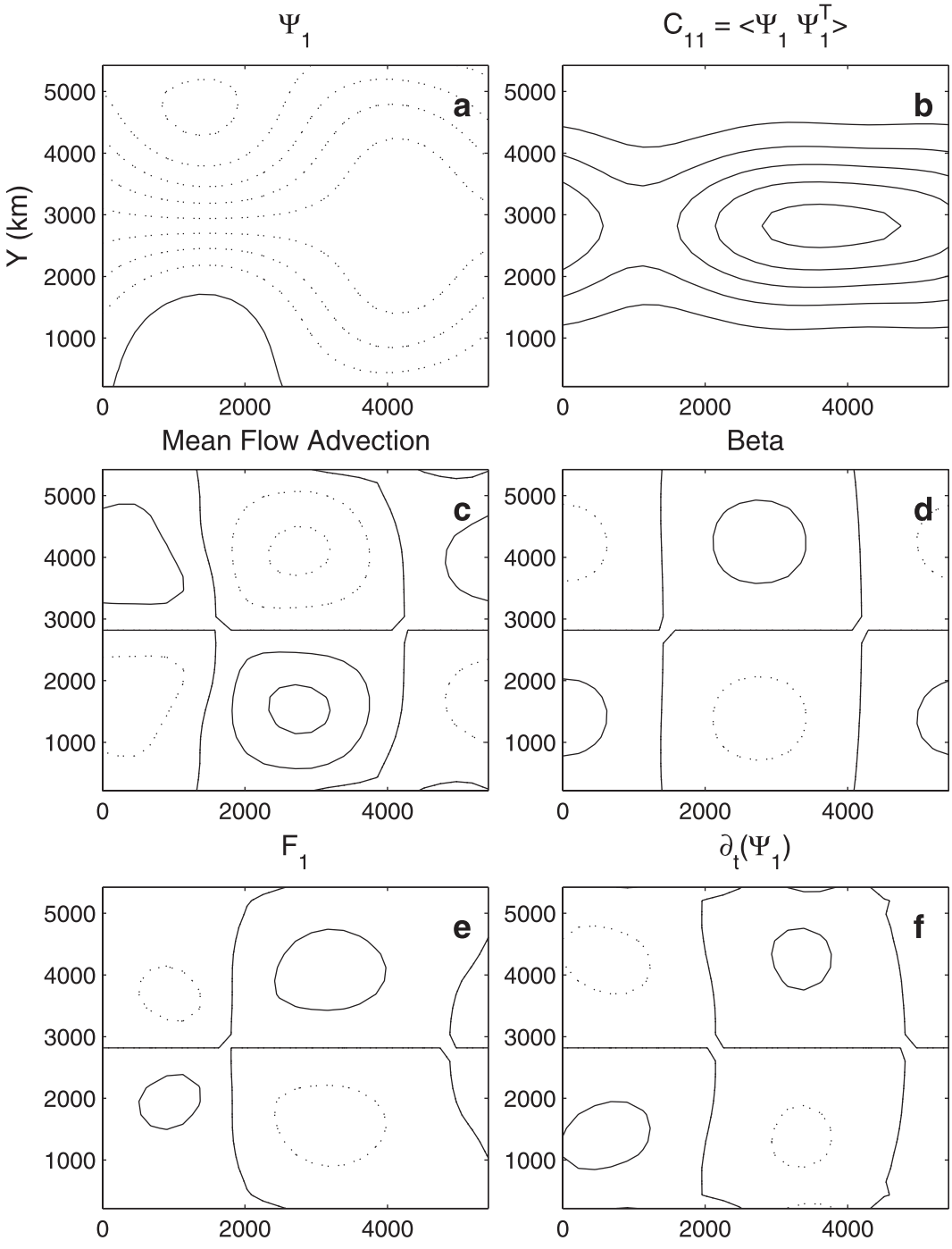

FIG. 9. As in Fig. 8, but for the minimum norm case.

confined by the meridional boundaries. The temporal variation of the block's growth and decay is measured by the frequency. As the excitation increases the cycle takes less time to complete. This results from the increase in strength of the turbulent fluxes forcing the block.

4. Discussion

We begin the discussion by comparing the results of our model with previous observations and calculations. Nakamura and Wallace (1990, 1993) shows that there is a marked enhancement of baroclinic wave activity

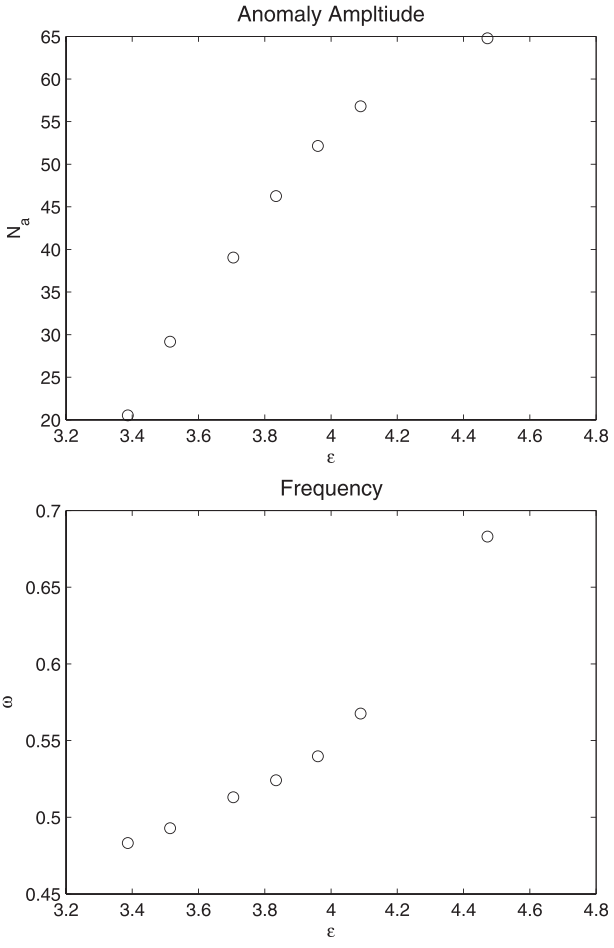

FIG. 10. Dependence of the limit cycle on ε: (a) amplitude of the zonal anomaly and (b) frequency of block growth and decay.

upstream from the block several days before the onset of a blocking event. They also show that a meridional flux of low PV low-latitude air by the eddies is responsible for the onset and maintenance of the block. This behavior is reflected in both our constant and oscillating block. In the constant block the eddy variance is upstream of the block, and during the spinup of the oscillating block the eddy variance concentrates upstream and becomes stronger. Our model also verifies that the fluxes from the turbulence are responsible for both the onset and maintenance of the block.

In addition to composite and statistical studies, Colucci (1985) presents detailed synoptic analyses of specific blocking events. He describes the evolution of a block in which a cyclone grows and propagates into a weak deformation region. A combination of vorticity and heat fluxes from the eddy act to enhance this system into the canonical dipole block, and as the cyclone propagates eastward the dipole pattern retrogresses. Although the presence of eddies is correlated with the onset of blocking, it is not a sufficient precursor. Colucci (2001) shows that in addition to synoptic-scale activity the mean flow must present a diffluence region to deform the eddies. In this way the mean flow influences the behavior of the eddies just as they force the mean flow. These studies all show properties similar to the results of our calculations. The retrogression of the block is seen in both the constant and oscillating block. The effect of the mean flow diffluence region is also evident in the oscillating block. As the eddy variance grows, the diffluence region amplifies, which causes the variance to concentrate farther upstream. Our calculations agree well with the observations, but it is also useful to compare them with geostrophically turbulent models.

Cai and Mak (1990) use a two-level β-channel model with rigid walls to study eddy–mean flow interactions. The meridional extent is similar to that of our model and the zonal extent is 5 times larger. Cai and Mak show that the turbulence forces a planetary-scale wave with $k = 2$ and $l = 2$. The maximum in eddy variance is located in the downstream portion of the jets for both models and the flow forced by the turbulence is upstream of the deformation it produces. When the forcing is split into baroclinic and barotropic components both contribute to maintaining the mean flow, with the barotropic part being stronger. This model has a geometry similar to ours and although the zonal wavenumber is larger, the physics of the planetary-scale wave is the same as ours. All calculations show that the turbulence forces the wave and the eddy variance is located upstream of the block. In addition, our Figs. 5b and 5d show that the relative magnitude of the heat and momentum fluxes is reproduced by our model.

The model employed by Cai and Mak (1990) is without doubt an overly simplified view of the atmosphere. More comprehensive but still relatively simple models using the primitive equations on a sphere all find a variety of low-frequency behavior, although the physics of the LFV can vary between models. For example, Branstator (1992) finds the turbulence produces mainly momentum fluxes, whereas Nigam et al. (1986) suggest that heat fluxes are necessary for maintaining large-scale waves. However, several common themes emerge. The transients always act to maintain the LFV and the LFV is equivalent-barotropic. The eddy variance is located in the exit regions of the jets and the forcing from turbulence and the mean flow advection cancel each other to a large degree (Robinson 1991; Branstator 1992). These properties are all shared with the model we present. Comparisons with both observations and geostrophically turbulent models show that the LFV produced by our model reproduces all of the previously observed and modeled physics. We now show how our model compares to other theories for blocking.

One theory for LFV in the atmosphere is based on the linear instability of zonally varying flows (Swanson 2002). Although this theory produces instabilities that resemble blocking patterns, the linear nature of the calculations does not allow for an obvious equilibration mechanism for the disturbances. Our model does not have this problem because the mean and perturbation equations are coupled so that they produce a consistent finite-amplitude equilibrium, which may be a fixed point or a limit cycle. Another candidate for explaining the LFV in the atmosphere is strongly nonlinear dipole eddies called modons (McWilliams 1980). Although these solutions resemble blocks, they lack a forcing mechanism to excite and maintain them. One proposed mechanism for the maintenance of modons is through transient eddy fluxes (Haines and Marshall 1987). However, in this study an artificial wavemaker is needed to generate the eddies that support the modon. In our model the turbulence is simulated using an extensively tested parameterization and the LFV is generated by a dynamically consistent field of eddies. Finally, there is the idea that the LFV can be explained either by multiple stable equilibria in the atmosphere (Charney and DeVore 1979) or by an exotic attractor in the dynamics (Crommelin 2003). Although multiple equilibria can be found in complex AGCMs, their relevance to geostrophically turbulent flows is difficult to establish. In addition, one would expect that a probability distribution function (PDF) associated with multiple equilibria would display multimodal behavior. However, all attempts to show this have been inconclusive (Berner and Branstator 2007).

To summarize the discussion, we have shown that the LFV generated by our model is consistent with the general characteristics of LFV simulated by AGCMs as well as a variety of observations. In addition, our model is able to provide a complete and consistent picture of the dynamics whereas other theories have a variety of shortcomings in the consistency of their dynamics.

5. Conclusions

We examine turbulence–mean flow interaction in a quasigeostrophic two-layer β-plane channel using a stochastic turbulence model. Equilibria formed by the turbulence and mean flow were examined as a function of the turbulence strength. Initially the flow remained zonal, but as the excitation increased the system underwent a bifurcation into a (1, 2) wave propagating upstream with a constant spatial structure. This wave is maintained by a three-way dynamical balance of the β effect, mean flow advection, and turbulent forcing. The phase speed of the wave is initially near zero and increases linearly, with the turbulence intensity controlled by the parameter ε. The amplitude of the wave also increases linearly with ε. Further increase of the bifurcation parameter results in a limit cycle in which the initially stationary block grows until it attains sufficient amplitude to begin propagating. This propagation causes the forcing to be out of phase with the block, which then decreases the block's amplitude, repeating the cycle.

Although the spatial structure of the LFV generated in this model resembles the observed and modeled blocking in the atmosphere, the model falls short in two aspects. The magnitude of the energy injection rate necessary to produce blocks is larger then the observed energy injection rate in the atmosphere, and irregular time-dependent variability is not reproduced. Time-dependent behavior consisting of the growth and decay of the block is observed, but the behavior is perfectly regular. The stochastic nature of cyclone formation precludes a limit cycle corresponding exactly to observed blocking. There have been many explanations put forth to describe the irregular nature of LFV. A strange attractor in the dynamics creating coherent structures with irregular phase space trajectories has been suggested (Crommelin 2003). However, implicit in this work is another candidate for the source of variability. The discussion of Reynolds averaging in section 2 points out that the assumptions needed to derive the Lyapunov Eq. (5) are never entirely met. This will result in stochastic fluctuations around the calculation using the infinite ensemble average. It will also result in stochastic fluctuations in the energy injection rate. It is possible that on average, the jet is in a zonal state while the stochastic fluctuations in eddy energy cause the jet to form blocks on occasion. The next step in this work is to use an explicitly stochastic model of eddy–mean flow interactions in the hope that it can reproduce the temporal statistics of blocking in the atmosphere.

Acknowledgments. This work was supported by NSF ATM-0736022.

APPENDIX

Scaling of Q

The excitation matrix $\mathbf{Q} = \mathbf{F}\mathbf{F}^{\mathrm{T}}$ is scaled so that $\varepsilon = 1$ corresponds to energy injection at rate 1 W m^{-2}. We would like $\mathbf{F}$ and therefore $\mathbf{Q}$ to be dimensionless, implying that ε has dimensions of m^4 s^{-3} according to the Lyapunov equation (5). To do this consistently requires defining the dimension of η to be s$^{-1/2}$ in

$$\frac{\partial \mathbf{p}}{\partial t} = \mathbf{A}\mathbf{p} + \varepsilon^{-1/2}\mathbf{F}\eta. \tag{9}$$

With variables carrying the correct dimensions, the stochastic energy injection rate is calculated using

$$E = -\frac{1}{2}\mathbf{p}^{\mathrm{T}}\mathbf{D}_{2f}\mathbf{p}\Delta x\Delta y\Delta z, \tag{10}$$

where Δx, Δy, and Δz are nondimensional grid spacing. Following DelSole (1996), an equation for the energy tendency can be derived by evaluating the expression

$$\mathbf{p}^{\mathrm{T}}\mathbf{D}_{2f}^{\mathrm{T}}\left(\frac{\partial\mathbf{p}}{\partial t}\right) + \left(\frac{\partial\mathbf{p}}{\partial t}\right)^{\mathrm{T}}\mathbf{D}_{2f}\mathbf{p}.$$

Using the identity

$$\mathbf{x}^{\mathrm{T}}\mathbf{Y}\mathbf{x} = \mathrm{trace}(\mathbf{Y}\mathbf{x}\mathbf{x}^{\mathrm{T}}),$$

where $\mathbf{x}$ is a vector and $\mathbf{Y}$ is a matrix, we obtain

$$-\frac{1}{2}\frac{\partial}{\partial t}(\mathbf{p}^{\mathrm{T}}\mathbf{D}_{2f}\mathbf{p}) = -\frac{1}{2}\,\mathrm{trace}[\mathbf{D}_{2f}(\mathbf{A}\mathbf{C} + \mathbf{C}\mathbf{A}^{\mathrm{T}} + \mathbf{Q})]. \tag{11}$$

The nondimensional stochastic energy injection rate is identified as

$$-\frac{1}{2}\,\mathrm{trace}(\mathbf{D}_{2f}\mathbf{Q}). \tag{12}$$

Multiplying (12) by $MU^3L_d^{-1}$, where $M = 1 \times 10^4$ kg m^{-2} is the mass per unit area of the atmosphere, gives an energy injection rate of 0.03 W m^{-2} for $\varepsilon = 1$. Therefore, we scale $\mathbf{Q}$ by the inverse of this so $\varepsilon = 1$ corresponds to an earth-equivalent energy injection rate of 1 W m^{-2}.

REFERENCES

Berner, J., and G. Branstator, 2007: Linear and nonlinear signatures in the planetary wave dynamics of an AGCM: Probability density functions. *J. Atmos. Sci.,* **52,** 117–135.

Branstator, G., 1992: The maintenance of low-frequency atmospheric anomalies. *J. Atmos. Sci.,* **49,** 1924–1946.

——, 1995: Organization of storm track anomalies by recurring low-frequency circulation anomalies. *J. Atmos. Sci.,* **52,** 207–226.

Cai, M., and M. Mak, 1990: Symbiotic relation between planetary and synoptic-scale waves. *J. Atmos. Sci.,* **47,** 2953–2968.

Carrera, M. L., R. W. Higgins, and V. Kousky, 2004: Downstream weather impacts associated with atmospheric blocking over the northeast Pacific. *J. Climate,* **17,** 4823–4839.

Chang, E. K. M., S. Lee, and K. L. Swanson, 2002: Storm track dynamics. *J. Climate,* **15,** 2163–2183.

Charney, J. G., and J. G. DeVore, 1979: Multiple flow equilibria in the atmosphere and blocking. *J. Atmos. Sci.,* **36,** 1205–1216.

Colucci, S. J., 1985: Explosive cyclogenesis and large-scale circulation changes: Implications for atmospheric blocking. *J. Atmos. Sci.,* **42,** 2701–2717.

——, 2001: Planetary-scale preconditioning for the onset of blocking. *J. Atmos. Sci.,* **58,** 933–942.

Crommelin, D. T., 2003: Regime transitions and heteroclinic connections in a barotropic atmosphere. *J. Atmos. Sci.,* **60,** 229–246.

D'Andrea, F., and Coauthors, 1996: Northern Hemisphere atmospheric blocking as simulated by 15 atmospheric general circulation models in the period 1979–1988. World Climate Research Programme, 22 pp.

DelSole, T., 1996: Can quasigeostrophic turbulence be modeled stochastically? *J. Atmos. Sci.,* **53,** 1617–1633.

——, 2004: Stochastic models of quasigeostrophic turbulence. *Surv. Geophys.,* **25,** 107–149.

——, and B. F. Farrell, 1995: A stochastically excited linear system as a model for quasigeostrophic turbulence: Analytic results for one- and two-layer fluids. *J. Atmos. Sci.,* **52,** 2531–2547.

Dole, R. M., 1986: Persistent anomalies of the extratropical Northern Hemisphere wintertime circulation: Structure. *Mon. Wea. Rev.,* **114,** 178–207.

——, and N. D. Gordon, 1983: Persistent anomalies of the extratropical Northern Hemisphere wintertime circulation: Geographical distribution and regional persistence characteristics. *Mon. Wea. Rev.,* **111,** 1567–1586.

Farrell, B. F., and P. J. Ioannou, 1993a: Stochastic dynamics of baroclinic waves. *J. Atmos. Sci.,* **50,** 4044–4057.

——, and ——, 1993b: Stochastic forcing of the linearized Navier–Stokes equations. *Phys. Fluids,* **5A,** 2600–2609.

——, and ——, 1994: A theory for the statistical equilibrium energy spectrum and heat flux produced by transient baroclinic waves. *J. Atmos. Sci.,* **51,** 2685–2698.

——, and ——, 1995: Stochastic dynamics of the midlatitude atmospheric jet. *J. Atmos. Sci.,* **52,** 1642–1656.

——, and ——, 1996: Generalized stability theory. Part I: Autonomous operators. *J. Atmos. Sci.,* **53,** 2025–2040.

——, and ——, 2003: Structural stability of turbulent jets. *J. Atmos. Sci.,* **60,** 2101–2118.

——, and ——, 2007: Structure and spacing of jets in barotropic turbulence. *J. Atmos. Sci.,* **64,** 3652–3665.

——, and ——, 2008: Formation of jets by baroclinic turbulence. *J. Atmos. Sci.,* **65,** 3353–3375.

Guckenheimer, J., and P. Holmes, 1983: *Nonlinear Oscillations, Dynamical Systems and Bifurcations of Vector Fields*. Springer-Verlag, 453 pp.

Haines, K., and J. C. Marshall, 1987: Eddy-forced coherent structures as a prototype of atmospheric blocking. *Quart. J. Roy. Meteor. Soc.,* **113,** 681–704.

Holopainen, E., and C. Fortelius, 1987: High-frequency transient eddies and blocking. *J. Atmos. Sci.,* **44,** 1632–1645.

——, L. Rontu, and N. C. Lau, 1982: The effect of large-scale transient eddies on the time-mean flow in the atmosphere. *J. Atmos. Sci.,* **39,** 1972–1984.

Holton, J. R., 1992: *An Introduction to Dynamic Meteorology*. 3rd ed. Academic Press, 511 pp.

Jin, F.-F., L.-L. Pan, and M. Watanabe, 2006: Dynamics of synoptic eddy and low-frequency flow interaction. Part I: A linear closure. *J. Atmos. Sci.,* **63,** 1677–1694.

Lorenz, D. J., and D. Hartmann, 2003: Eddy–zonal flow feedback in the Northern Hemisphere winter. *J. Climate,* **16,** 1212–1227.

McWilliams, J. C., 1980: An application of equivalent modons to atmospheric blocking. *Dyn. Atmos. Oceans,* **5,** 43–66.

Nakamura, H., and J. M. Wallace, 1990: Observed changes in baroclinic wave activity during the life cycles of low-frequency circulation anomalies. *J. Atmos. Sci.,* **47,** 1100–1116.

——, and ——, 1993: Synoptic behavior of baroclinic eddies during the blocking onset. *Mon. Wea. Rev.,* **121,** 1892–1903.

Nigam, S., I. M. Held, and S. W. Lyons, 1986: Linear simulation of the stationary eddies in a general circulation model. Part I: The no-mountain model. *J. Atmos. Sci.,* **43,** 2944–2961.

Notaro, M., W. C. Wang, and W. Gong, 2006: Model and observational analysis of the Northeast U.S. regional climate and its relationship to the PNA and NAO patterns during early winter. *Mon. Wea. Rev.,* **134,** 3479–3505.

Robinson, W. A., 1991: The dynamics of low-frequency variability in a simple model of the global atmosphere. *J. Atmos. Sci.,* **48,** 429–441.

Shutts, G. J., 1983: The propagation of eddies in diffluent jetstreams: Eddy vorticity forcing of 'blocking' flow fields. *Quart. J. Roy. Meteor. Soc.,* **109,** 737–761.

Simmons, A. J., J. M. Wallace, and G. Branstator, 1983: Barotropic wave propagation and instability and atmospheric teleconnection patterns. *J. Atmos. Sci.,* **40,** 1363–1392.

Swanson, K. L., 2002: Dynamical aspects of extratropical tropospheric low-frequency variability. *J. Climate,* **15,** 2145–2162.

Whitaker, J. S., and A. Barcilon, 1995: Low-frequency variability and wavenumber selection in models with zonally symmetric forcing. *J. Atmos. Sci.,* **52,** 491–503.

——, and P. D. Sardeshmukh, 1998: A linear theory of extratropical synoptic eddy statistics. *J. Atmos. Sci.,* **55,** 237–258.

Zhang, Y., and I. M. Held, 1999: A linear stochastic model of a GCM's midlatitude storm tracks. *J. Atmos. Sci.,* **56,** 3416–3435.